Draft version January 10, 2020
Typeset using LaTeX default style in AASTeX62

Onset and evolution of the oblique, resonant electron firehose instability in the expanding solar wind plasma

Maria Elena Innocenti,[1] Anna Tenerani,[2] Elisabetta Boella,[3, 4] and Marco Velli[5]

[1] Jet Propulsion Laboratory, Interstellar and Heliospheric Physics Division, 4800 Oak Grove Dr, Pasadena, CA 91109
[2] Department of Physics, The University of Texas at Austin, TX 78712
[3] Lancaster University, Physics Department, Bailrigg, Lancaster LA1 4YW, UK
[4] Cockcroft Institute, Sci-Tech Daresbury, Keckwick Lane, Warrington WA4 4AD, ,UK
[5] University of California Los Angeles, Department of Earth, Planetary, and Space Sciences, 595 Charles E Young Dr E, Los Angeles, CA 90095

Submitted to ApJ

ABSTRACT

A double-adiabatically expanding solar wind would quickly develop large parallel to perpendicular temperature anisotropies in electrons and ions, that are not observed. One reason is that firehose instabilities would be triggered, leading to an ongoing driving/saturation evolution mechanism. We verify this assumption here, for the first time, for the electron distribution function and the electron firehose instability (EFI), using fully kinetic simulations with the expanding box model. This allows the self-consistent study of onset and evolution of the oblique, resonant EFI in an expanding solar wind. We characterize how the competition between EFI and adiabatic expansion plays out in high- and low-beta cases, in high and low speed solar wind streams. We observe that, even when competing against expansion, the EFI results in perpendicular heating and parallel cooling. These two concurrent processes effectively limit the expansion-induced increase in temperature anisotropy and parallel electron beta. We show that the EFI goes through cycles of stabilization and de-stabilization: when higher-wavenumber EFI modes saturate, lower-wavenumber modes are destabilized by the effects of the expansion. We show how resonant wave-particle interaction modifies the electron eVDF after the onset of the EFI. The simulations are performed with the fully kinetic, semi-implicit Expanding Box code EB-iPic3D.

Keywords: instabilities, plasmas, methods: numerical, Sun: heliosphere, solar wind

1. INTRODUCTION

In the solar wind, both ion and electron velocity distribution functions (VDFs) exhibit kinetic, non-thermal features, which evolve with heliocentric distance due to a combination of expansion, nonlinearities and kinetic instabilities (Pilipp et al. 1987; Maksimovic et al. 2005; Marsch 2012). The electron VDF is composed of three populations: core, halo and beam ("strahl"). The core is colder, with Coulomb collisions possibly reducing its $T_\parallel/T_\perp$ anisotropy to the lowest values observed among solar wind electron populations (Feldman et al. 1975) (T is the temperature, the subscript refers to the direction with respect to the background magnetic field). The hotter halo is definitely collisionless and exhibits larger values of $T_\parallel/T_\perp$ thermal anisotropy. In this case, the anisotropy values are supposedly controlled by wave/particle interaction processes (Feldman et al. 1975). The strahl is a beam of field-aligned, (most of the time) anti-Sunward directed electrons, whose angular width changes as a function of solar wind conditions and heliocentric distance, most probably due to wave/particle scattering processes (Hammond et al. 1996; Maksimovic et al. 1997). Strahl electrons appear to scatter into the halo at increasing heliocentric distances (Maksimovic et al. 2005).

The non-equilibrium, non-thermal nature of the eVDF suggests that kinetic, collisionless processes may play a role in electron solar wind dynamics. This intuition is strengthen by observations in both slow and fast streams that show that

Corresponding author: Maria Elena Innocenti
maria.elena.innocenti@jpl.nasa.gov

the solar wind electron VDF is bounded by kinetic instabilities (notably temperature anisotropy driven instabilities) in the parameter space $T_\parallel/T_\perp$ vs $\beta_\parallel$, where β is the ratio of plasma to magnetic pressures (Hellinger et al. 2006; Štverák et al. 2008; Matteini et al. 2013). It is assumed that when a plasma parcel close to marginal stability "leaves" the stable region, it is quickly brought back to it by the onset and saturation of the relevant instability.

Solar wind electrons (and in particular, slow wind core electrons) appear to be bounded by the whistler instability in the $T_\perp > T_\parallel$ regime, and by the electron firehose instability (EFI) in the $T_\parallel > T_\perp$ case (Štverák et al. 2008). In this paper, we will self-consistently study the onset and evolution of the oblique resonant electron firehose instability in the expanding solar wind plasma.

We focus here on oblique, rather than parallel, propagation, because the oblique EFI has lower threshold and higher growth rate with respect to the parallel (Li & Habbal 2000; Paesold & Benz 1999; Gary & Nishimura 2003; Camporeale & Burgess 2008): the oblique, not parallel, EFI arises self-consistently in our simulations. The oblique EFI is generally considered purely growing, while the parallel EFI exhibits a real frequency component. According to Li & Habbal (2000), a real frequency component is expected at $\theta < 30°$, where θ is the propagation angle with respect to the background magnetic field. Camporeale & Burgess (2008) move the limit up to $\theta \sim 50°$.

Parallel and oblique EFI differ also in the nature of wave/particle interactions. A number of studies (Paesold & Benz 1999; Li & Habbal 2000; Messmer 2002; Gary & Nishimura 2003) have focused on the electron heating mechanism in parallel and oblique propagation. Calculating the resonance factor for ions and electrons, they conclude that the parallel electron firehose instability is not resonant for electrons (unless the temperature anisotropy is very high), while the oblique EFI is. Messmer (2002), however, shows that this distinction is not so clear-cut: in his 1D3V simulation of parallel firehose instability, he sees clear signs of anomalous Doppler resonance. He concludes that the parallel firehose instability he observes is still non resonant because the bulk of the perpendicular heating is achieved through non resonant, rather than resonant, wave particle interaction. Non resonant interaction is not $v_\parallel$ specific, while resonant, anomalous Doppler interaction heats preferentially particles with parallel velocity $v_\parallel \sim \pm\Omega_{ce}/\sqrt{2}k_\parallel d_e$, where Ω_{ce} is the electron cyclotron frequency, k the wavenumber and d_e the electron skin depth.

Notwithstanding the nature of the heating, however, both parallel and oblique EFI heat electrons in the perpendicular direction while there is cooling in the parallel direction, causing a decrease in the parallel beta. Recent work has focused on parallel electron and ion FI-mediated electron/ion interaction and on its impact on the VDFs of the two particle species (?).

The development of kinetic instabilities in general and of the EFI in particular depends on the evolution of the solar wind bulk parameters with heliocentric distance R. Solar wind expansion naturally induces strong temperature anisotropies in the $T_\perp/T_\parallel < 1$ direction, driving the plasma towards firehose-type instability. This can be easily understood assuming conservation of the two adiabatic invariants $T_\perp/B$ and $T_\parallel B^2/n^2$, as described by the CGL model (Chew et al. 1956). Because in a spherically expanding wind density and radial magnetic field evolve as $B_x, n \propto R^{-2}$ (see Behannon (1978); Matteini et al. (2013); Hellinger et al. (2011); Štverák et al. (2015) for observed radial trends), the following dependences for perpendicular and parallel temperatures and for the parallel plasma beta are expected $\beta_\parallel$: $T_\perp \propto R^{-2}$, $T_\parallel = const$, $\beta_\parallel \propto R^2$.

Such radial evolution however, is generally not verified in observations (Matteini et al. 2013), most probably because of the development of perpendicular heating and parallel cooling processes and the onset of instabilities and wave-particle resonances not described by the CGL approximation. Simple back-of-the-envelope calculations can clarify this statement. In a spherically expanding plasma, gyrofrequencies decline as R^{-2}, the dependence with R of the dominant (at least close the Sun), average radial magnetic field component. The eigen-frequencies of a number of waves depends on the plasma parameters in such a was as to decay more slowly with R, e.g. $\omega \propto 1/R$ for Alfvén waves. Hence, waves evolve into regimes where kinetic effects increase in importance, so that wave-particle interactions and the perpendicular heating they produce are expected to become a more frequent occurrence with increasing heliocentric distances. Similar considerations hold for kinetic instabilities. Plasma expansion increases the parallel plasma beta and decreases the $T_\perp/T_\parallel$ ratio. This means that an expanding plasma parcel comoving with the wind and initially in stable conditions may cross the instability threshold for a number of electromagnetic instabilities (most notably the electron firehose instability, EFI).

These two classes of processes (resonances and instabilities induced by expansion) have been studied for ion distribution functions via numerical simulations, in Liewer et al. (2001) and Matteini et al. (2006); Hellinger et al. (2003) respectively. In Hellinger et al. (2015), the competition between perpendicular proton heating due to decaying turbulence and perpendicular cooling from expansion has been investigated. All these simulations have been performed with an hybrid implementation of the Expanding Box Model (EBM), previously developed in a MagnetoHydroDynamics (MHD) framework by Grappin & Velli (1996); Velli et al. (1992).

The EBM is designed to describe the dynamics of a small sector of plasma (the simulation box) which is in spherical expansion as it is comoving, with speed $\mathbf{U}'$, with the average solar wind outflow. The change of frame of reference from a Sun-centered frame ($\mathbf{x}'$) to a co-moving frame ($\mathbf{x}$) allows the evolution of such a plasma sector to be followed in a semi-lagrangian fashion by accounting for expansion effects via an explicit dependence on the average heliocentric distance $R(t)$. The latter is taken along the x' direction and can be considered as the lagrangian variable of the background solar wind, evolving as $R(t) = R_0 + U_0 t$. Both R_0 and U_0 are free parameters of the system and $R_0/U_0 = \tau_e$ defines the expansion timescale. In the formulation used here, U_0 is constant, but solar wind acceleration can also be introduced (Tenerani & Velli 2017). The EBM describes the dynamics occurring on timescales shorter than τ_e in a locally plane geometry (i.e. curvature effects are neglected on the box scale) while the effects of the expansion are taken into account as slow time-variations of average quantities via a parametric dependence on $R(t)$.

The MHD implementation of the EBM targets large-scale, sometimes heliospheric-wide, processes, e.g. Dong et al. (2014); Verdini & Grappin (2015, 2016). The above-mentioned EBM hybrid implementation (as the recent one described in Ofman (2019)) focuses on ion scale processes. In this paper, for the first time, we present simulations of the *electron* firehose instability (EFI) in the expanding solar wind plasma. The simulations are done with the recently implemented fully kinetic, semi-implicit Expanding Box Model code EB-iPic3D (Innocenti et al. 2019).

EB-iPic3D introduces the EBM concept into the Implicit-Moment-Method, IMM (Brackbill & Forslund 1982; Lapenta et al. 2006), Particle-In-Cell (PIC) code iPic3D (Markidis et al. 2010). Thanks to the semi-implicit IMM temporal discretization, the temporal and spatial resolution of the code can be adapted to the scale of the processes under investigation rather than being tied to the strict stability constraints of explicit discretizations. This property is massively exploited in the Multi-Level Multi-Domain evolution of iPic3D, where several grid levels are resolved with different spatial and temporal resolutions to catch progressively smaller scale processes (Innocenti et al. 2013, 2015, 2016). Other, non semi-implicit, fully kinetic implementations of similar EB formulations are Sironi & Narayan (2015) and Ahmadi et al. (2017), where the compression (rather than expansion) of the plasma mimics collisionless accretion flow and magnetopause compression respectively.

In Innocenti et al. (2019), the equations of the EBM IMM method and the unique challenges coming from discretizing semi-implicitly the PIC EB equations are detailed. Simple 1D3V tests verified the double adiabatic evolution of magnetic field and thermal parallel and perpendicular velocities. Since the focus was on the double adiabatic evolution, kinetic instabilities outside of the scope of the CGL approximation were purposefully suppressed numerically. In the unmagnetized plasma case, the Weibel instability (Weibel 1959; Innocenti et al. 2011) was suppressed by means of the 1D geometry: the wavenumber of the Weibel instability is in the direction of the "cold" thermal velocities, hence in the transverse direction in an EB simulation. In Innocenti et al. (2019), only the radial direction was simulated. In the magnetized plasma case, the electron parallel firehose instability was quenched by simulating a box too small to fit the large wavelength of the parallel firehose instability (Gary 2005; Messmer 2002). The oblique electron firehose instability (Gary & Nishimura 2003; Camporeale & Burgess 2008; Hellinger et al. 2014) was also suppressed due to the lack of (at least partially) transverse wavenumbers.

In this work, we move beyond double-adiabatic evolution by allowing electron instabilities to be triggered. To do so, we carry out 2D3V simulations with relatively large box sizes, $L_x/d_e = L_y/d_e = 160$ at initialization, with d_e the electron skin depth calculated with respect to the initial plasma parameters. With a 2D3V simulation geometry and access to low wavenumber, the oblique firehose instability develops when a sufficiently high electron thermal anisotropy is reached due to the expansion.

Before proceeding, we notice again that, in order to study the development of the EFI, we simulate our electrons kinetically via a fully kinetic, PIC approach. PIC codes generally assume that Coulomb collisions have little effect with respect to wave/particle interaction processes both in modifying the electron and ion VDFs and in controlling the heat flux.

Already at the time of the Mariner 10 mission, negligible energy exchange through Coulomb collisions between the core and halo population was assumed, and the existence of correlated variations in core and halo temperature with heliocentric distance was instead attributed either to temporal coronal source variations or to wave/particle coupling (Ogilvie & Scudder 1978). Regarding the role of collisions in shaping the single electron populations, Ogilvie & Scudder (1978) compared the calculated characteristic collisional lengths and density scale heights and concluded that collisions may be relevant for core (at least at $R < 1\,\mathrm{AU}$) but not for halo dynamics.

In Scime et al. (1994), the solar wind heat flux was calculated from Ulysses observations between 1 and 5 AU, and found to have lower values than those expected for a collisional heat flux due to thermal conductivity: wave/particle processes, rather than collisions, were then invoked as heat flux regulators. In Salem et al. (2003), an inverse correlation was observed between the collisional age of the plasma and the level of thermal anisotropy of the electron population; among other things, this explains why the fast wind ("collisionally younger") expresses more pronounced kinetic characteristics with respect to the slow wind. In the same work, a relation was found (at least in certain solar wind regimes) between the upper bound of the observed heat flux and the collisional age, hinting at a non negligigle role of Coulomb collisions in regulating the heat flux. More recently, in Wilson III et al. (2018), a comparison has been carried out between the Coulomb collision rates (dominated by electron-electron and electron-proton processes) and the effective wave-particle interaction rates between electrostatic ion-acoustic waves and particles for 10 years of Wind observations near 1 AU. The ion acoustic wave was used as a sort of standard-bearer for kinetic processes because, a) it is often observed, and b) there is an analytical expression for its collision rate comprised of measurable parameters common in the solar wind. It stands to reason that other kinetic processes would exhibit comparable effective collision rates. The median values of the ratio of the ion acoustic to Coulomb collision rates is $> 10^2$, highlighting the fundamental role of kinetic processes in shaping solar wind parameters even at 1 AU, i.e. relatively close to the Sun.

In summary, observational evidence points to a coexistence of collisional and collisionless processes in shaping electron solar wind dynamics (ions can be considered collisionless starting from very low heliocentric distances). The relative weight of the two mechanisms changes with heliocentric distance, electron population, wind regimes (the fast wind exhibits more distinctly kinetic features, such as more prominent velocity tails (Maksimovic et al. 1997) and more compact strahl (Fitzenreiter et al. 1998), which point to a larger degree of collisionless behavior). As one could reasonable expect, kinetic characteristics are more pronounced in cases (fast vs slow wind, halo vs core) where collisional length-scales are larger. In those cases in particular, we can expect the majority of energy redistribution within the population to be mediated by wave/particle interaction processes, rather than by Coulomb collisions. These are the more direct targets of our present investigation, conducted with a PIC approach where Coulomb collisions are not implemented.

Fully kinetic simulations of solar wind electron dynamics, however, are of relevance also for solar wind conditions where the boundary between collisional and collisionless behavior is not so clear-cut. Fully kinetic investigations can then be used to estimate the level of population isotropization and the relative spatial and temporal scale that one can expect from a certain collisionless process. Values so obtained could then be compared with those expected from collisional processes, to determine which energy redistribution model fits better with the relevant observations.

As a final thought on the topic, we remark on the possibility of studying the competition of collisional and collisionless processes self-consistently, via the introduction of a Coulomb collisional operator in a PIC code as done, for example, in Daughton et al. (2009). There, the aim was to investigate the transition between magnetic reconnection regimes dominated by collisionless and collisional processes. A similar evolution of our code is left as future work.

The structure of the paper is as follows: in Section 2 we describe the simulation setup, parameter and overall evolution. In Section 3 we focus on the evolution of the electron velocity distribution with heliocentric distance. Conclusions are drawn in Section 4.

2. SIMULATED SETUP AND GLOBAL EVOLUTION

We present four 2D3V fully kinetic expanding box model simulations, initialized with the adimensional parameters shown in Table 1. $v_{th,e}$ is the electron thermal velocity normalized to the speed of light c. U_0 is the radial background solar wind speed, kept constant during the simulation. β_e is the electron plasma beta at the beginning of the simulation, when the electron velocity distribution functions are isotropic. The lines in 1 labelled as "SIM" refer to our simulations. The last two lines are solar wind conditions at 0.25 and 1 AU, compatible with Štverák et al. (2008). Comparing the six lines, one can see that our initial parameters are quite compatible, especially in the case of the low-beta simulations, with actual solar wind parameters. The expansion time scale $\tau_e = R/U_0$, controlling the variation of the simulation parameters with heliocentric distance, is chosen to be shorter than in reality (i.e. the initial heliocentric distance is quite low) to speed up the effects of expansion in the simulations. It is, however, slower than the characteristic evolution time of the instabilities investigated in the rest of the paper. The low- and high-wind speed cases correspond, in real units, to wind speeds of the order of ~ 400 and ~ 800 km/s respectively, i.e. slow and fast solar wind conditions. From the $U_0/v_{th,e}$ column of Table 1, we can see that the thermal velocity of electrons is larger than the solar wind speed: the wind is subsonic for electrons, while it is supersonic for ions. We will comment on the implications of this for our fully kinetic PIC approach in the Conclusions. The last two columns of Table 1 will be useful in the rest of the paper, as they show the letter and color associated to each simulation in the plots.

Other simulation parameters, common to the four simulations, are $T_i = T_e$, $L_x/d_e = L_y/d_e = 160$, $dx/d_e = dy/d_e = 0.625$, $\omega_{pe}dt = 0.4$, $m_r = 1836$, $R_0/d_e = 100$, where T is again the temperature, L is the box size at initialization, normalized to the electron skin depth d_e, dx, dy are the spatial resolutions, dt the temporal resolution, ω_{pe} the electron plasma frequency, m_r the ion (i) to electron (e) mass ratio and R_0 the initial radial position of the expanding box with respect to the Sun. 576 particles per species per cell are used. At initialization, the electron and ion velocity distribution functions are isotropic and only a radial magnetic field component is present. The box length $L_x/d_e = L_y/d_e = 160$ is chosen to accommodate the relatively low wavenumber characterizing the oblique firehose instability.

Table 1. Key adimensional solar wind parameters at initialization in our simulations (SIM 1 to 4) and in the solar wind at 0.25 and 1 AU

	$v_{th,e}/c$	$U_0/v_{th,e}$	β_e	panel	color
SIM 1	0.05	0.5	0.52	**a**	red
SIM 2	0.05	0.25	0.52	**b**	magenta
SIM 3	0.05	0.5	2.08	**c**	black
SIM 4	0.05	0.25	2.08	**d**	blue
0.25 AU	0.01	0.23	0.21	-	-
1 AU	0.007	0.36	0.66	-	-

The two simulated directions are the radial, x, and one of the two transverse, y, co-moving directions. The co-moving coordinates (i.e., the simulated coordinates, $\mathbf{x}$) map to the Sun-centered coordinates, $\mathbf{x}'$, as

$$x = x' - R(t), \quad y = y' R_0/R(t), \quad z = z' R_0/R(t), \tag{1}$$

This means that, at the end of the simulation, the box length in the x direction is the same, both in co-moving and in Sun-centered coordinates. The box length in the y direction, instead, has increased by a factor $R_f/R_0 \sim 10$ in the Sun-centered coordinate system (the duration of all simulations is adjusted as to reach the same final heliocentric position, $R_f/d_e \sim 1000$), while remaining the same in the co-moving coordinate system. The plots in this paper are in the co-moving coordinate system, unless otherwise specified, as in Figure 2 and Figure 6, panel c and d.

In all the simulations presented, the initial background solar wind magnetic field is purely radial, B_x. Hence, in this paper, “radial” and “parallel”, and “transverse” and “perpendicular”, have respectively the same meaning.

The spatial and temporal normalizations used in this paper are as follows: distances are normalized to the electron skin depth d_e, while times are normalized to the electron plasma frequency ω_{pe}, both calculated at initialization. Since the density varies with heliocentric distance as $n \propto R^{-2}$, the electron skin depth and plasma frequency vary as a function of R as $d_e(R) = d_e\ R/R_0$ and $\omega_{pe}(R) = \omega_{pe}\ R_0/R$ respectively. When the R dependence is omitted and if not otherwise specified, d_e and ω_{pe} are to be intended as the ones at $R = R_0$.

In Figure 1 we show δB_x as a function of heliocentric distance R/d_e and of the co-moving y/d_e coordinates for the four simulations mentioned above. δB_x are the oscillations over the background value of the normalized radial magnetic field, $B_x/(4\pi m_e c^2 n_0)^{1/2}$. All the panels are cuts at $x/d_e = L_x/2$. The bulk value of the radial magnetic field evolves with heliocentric distance as R^{-2}; the oscillations $\delta B_x(t) = B_x(t) - \bar{B}_x(t)$, where $\bar{B}_x$ is the average in the x and y directions at a specific time t, are depicted in the Figure. Notice that the oscillations in the out-of-plane magnetic field B_z are larger than δB_x (not of B_x) after instability onset. However, in this paper, we focus mostly on the evolution of B_x because it offers the occasion to appreciate the expansion-induced variation with heliocentric distance of the mean value of B_x, to which the firehose-generated δB_x oscillations superimpose. Additionally, parallel fluctuations confirm our identification of the instability as an oblique, rather than parallel, firehose instability.

All four cases display an overall similar behavior: low magnitude δB_x oscillations become larger magnitude oscillations after the onset of the instability, which is marked by a vertical dotted line at $R/d_e \sim 420, 356, 196, 164$ respectively. The heliocentric distance of instability onset (or better in this case, the last stable point) is identified by the sudden variation in the coupled parallel / perpendicular thermal velocity behavior better investigated later in Figure 4.

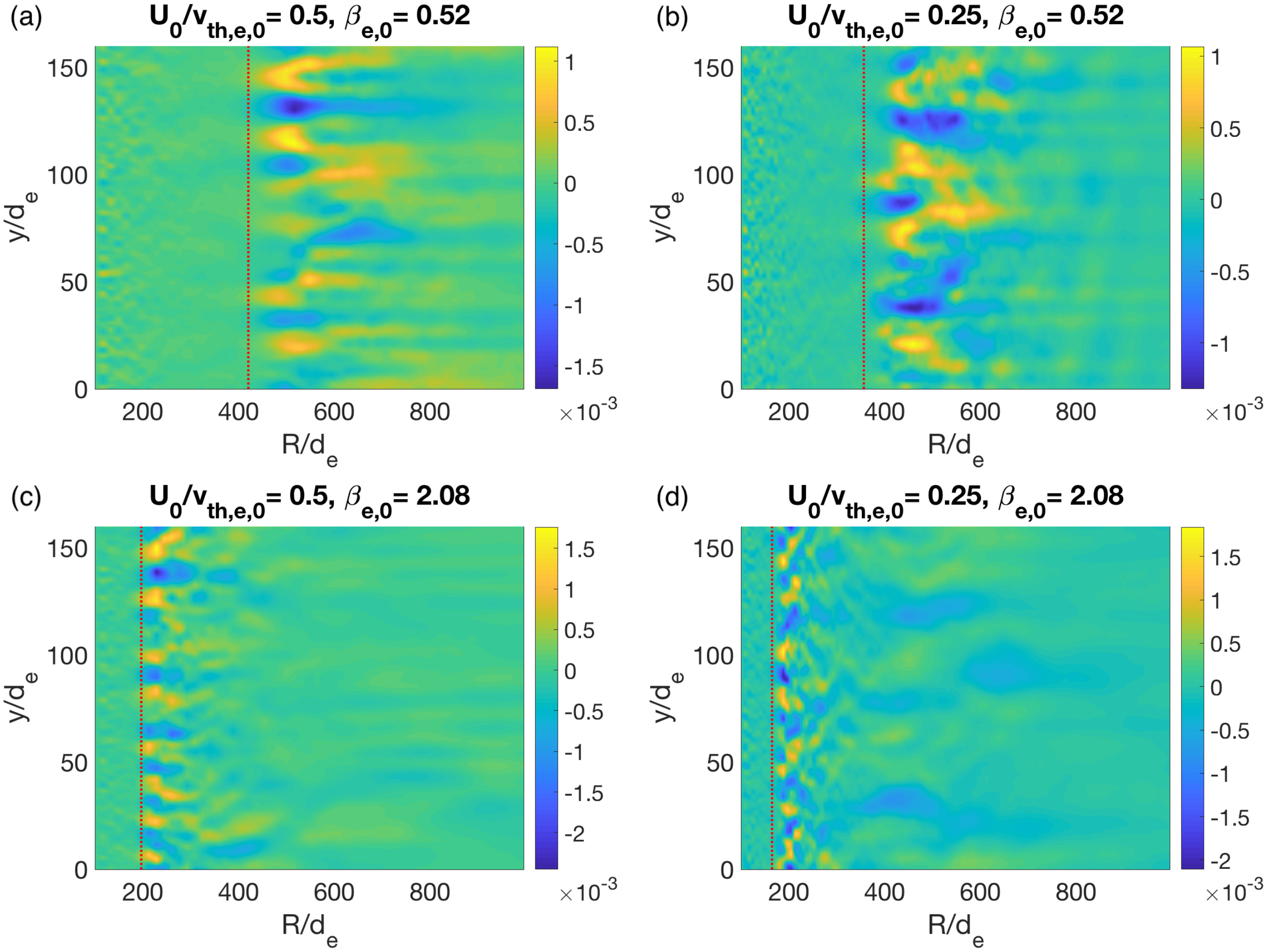

Figure 1. Evolution as a function of heliocentric distance, R/d_e, and co-moving y coordinate, y/d_e, of δB_x (x is the radial direction) at $x/d_e = L_x/2$ for the four simulations under investigation. The simulation parameters at initialization (hence the subscript 0) are reported above the respective panels. The dotted vertical lines at $R/d_e \sim 420, 356, 196, 164$ respectively mark the heliocentric distance of instability onset (or better, the heliocentric distance of the last stable point), as identified in Figure 4.

After reaching a peak value, the oscillations start decreasing in magnitude and then give rise to a slightly different evolution in the different cases. In panel b, we observe the emergence of real frequency oscillations beginning approximately at $R/d_e \sim 400$. In panel c and d, the wavelength of the instability in the perpendicular direction appears to decrease at later times in the comoving frame.

In Figure 2 we show a plot of the B_x field in the four cases, immediately after the onset of the instability. In this case, the plot coordinates are in the Sun-centered system, rather than in the co-moving system as before, to show how the box has stretched in the transverse direction since the beginning of the simulation. The lines superimposed on the plots allow to visually identify the inclination with respect to parallel propagation of the most unstable modes immediately after instability onset. The magenta, dotted red, blue and solid red lines corresponds to a propagation angle with respect to the parallel direction (x) of $\theta \sim 10, 30, 45, 80°$. We can guess from these plots (and we confirm it through a spectral analysis, where we take into account the variation of the transverse wavenumber with box expansion) that the firehose instability which develops is oblique rather than parallel. This is expected, since, as we remarked in the Introduction, the oblique firehose instability has lower threshold and higher growth rate than the parallel (Li & Habbal 2000; Paesold & Benz 1999; Gary & Nishimura 2003; Camporeale & Burgess 2008). In particular the propagation angle at instability onset is $\theta \sim 45,\ 45,\ 50,\ 50°$. When multiple, contiguous wavenumbers are unstable, we have taken the central wave vector as reference to calculate the angle.

In Figure 2, the dotted red line corresponds to $\theta \sim 30°$. According to Li & Habbal (2000), a real frequency component should arise for propagation angles $\theta < 30°$, i.e. in the quasi-parallel, propagating limit. Camporeale & Burgess (2008), however, observes real frequency components up to $\theta \sim 50°$.

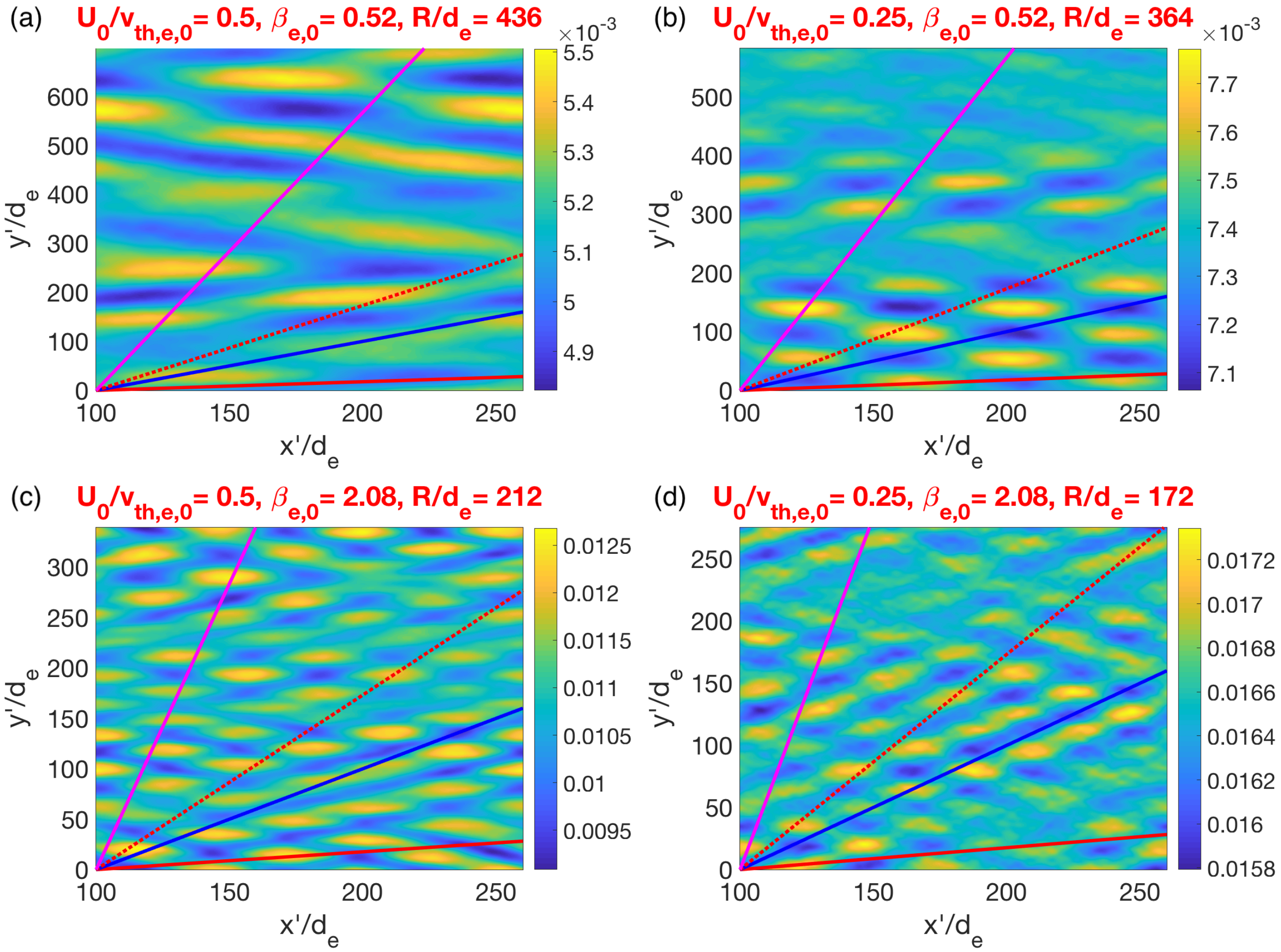

Figure 2. B_x magnetic field component, immediately after instability onset, for the four simulations of Figure 1. The spatial coordinates are in the Sun-centered, rather than comoving, system. The magenta, dotted red, blue and solid red lines corresponds to a propagation angle with respect to the parallel direction (x) of $\theta \sim 10, 30, 45, 80°$. θ is the propagation angle with respect to the radial direction (here, also the direction of the background magnetic field) in the k_x vs k_y plane, see e.g. panel a and b in Figure 4 for a visual representation.

In Figure 1, real oscillations in heliocentric distance (and hence, in time), are visible in panel b. As remarked earlier, the angle of propagation at instability onset in this case is $\theta \sim 45°$ (hence below the $\theta \sim 50°$ limit, consistently with Camporeale & Burgess (2008)).

Comparing again the four panels in Figure 1, one can also see that the perpendicular wavelength and heliocentric distance of instability onset depend more on the initial beta than on the initial wind speed. The lower-beta simulations (panel a and b in Figure 1) go unstable later in heliocentric distance and at larger transverse wavenumber than the higher-beta simulations, panel c and d.

To get a better understanding of instability onset, we plot the trajectory of the four simulations in the $T_{\perp,e}/T_{\parallel,e}$ vs $\beta_{\parallel,e}$ plane in Figure 3. The reader can refer to the Figure legend and to Table 1 to map each simulation to the corresponding line.

All simulations start from isotropic initial conditions, $T_{\perp,e}/T_{\parallel,e} = 1$. The red and magenta and black and blue lines are the low and high beta simulations respectively. The red and black and magenta and blue lines are the high and low U_0 cases. The dots mark the same simulation time, $\omega_{pe}t \sim 36000$, which corresponds respectively to the final time and half of the simulation for the high and low U_0 cases. The dotted, dashed, solid black curves are the isocontours of growth rates $\gamma/\Omega_{ce} = 0.001, 0.1, 0.2$ for the resonant (i.e. oblique) EFI, from Gary & Nishimura (2003). The isocontour at $\gamma/\Omega_{ce} = 0.001$ is often consider the marginal stability curve, dividing the $T_{\perp,e}/T_{\parallel,e}$ vs $\beta_{\parallel,e}$ space into oblique firehose stable (above the curve) and unstable (below).

The green lines are the trajectory on the plane expected from purely double-adiabatic expansion.

We see that all four simulations expand double-adiabatically before instability onset. At that stage, in fact, the assumptions of CGL are still valid in the simulations. The electron firehose instability results in perpendicular heating and parallel cooling. This breaks the CGL assumptions, and in fact the onset of the instability is quite evidently marked by departure from double-adiabatic behavior. Reasonably, in all cases, instability onset occurs under the firehose instability threshold. Higher-beta plasmas start the simulation closer to the instability threshold and, as observed in Figure 1, go unstable at lower Rs. Lower U_0 simulations, magenta and blue lines, depart earlier from the green lines with respect to their faster counterparts: faster wind means that the distribution functions can plunge further into the unstable region before being lifted away by the instability.

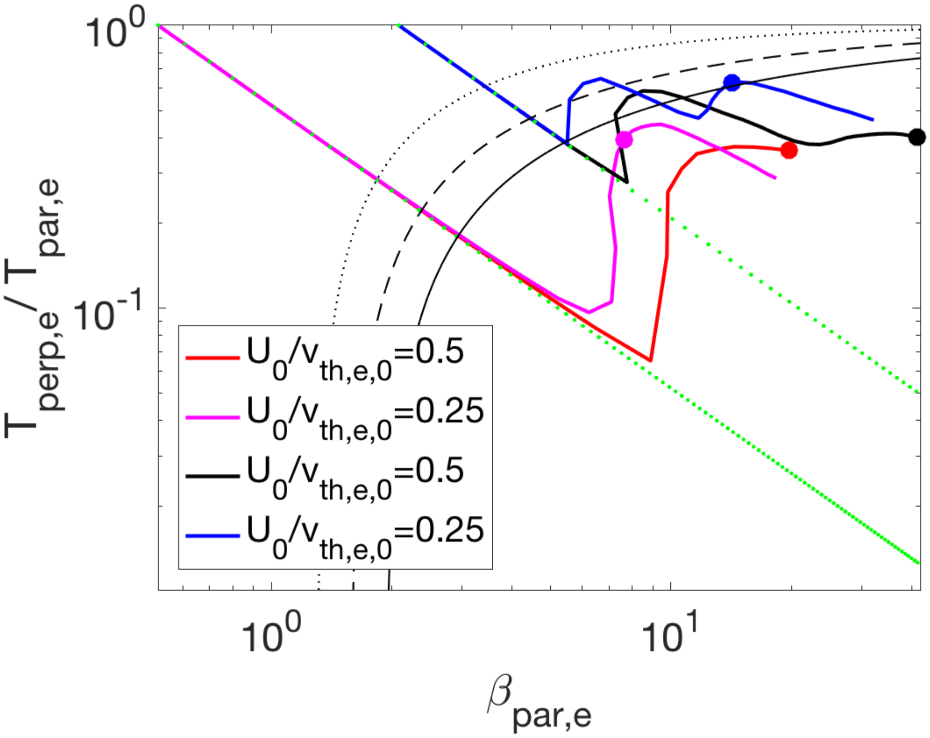

Figure 3. Simulation trajectory in the $T_{\perp,e}/T_{\parallel,e}$ vs $\beta_{\parallel,e}$ plane. The wind speed is reported in the legend. The red and magenta lines are the lower-beta, the black and blue lines the higher-beta simulations. The green lines mark double adiabatic expansion for the two classes of simulations. All simulations start and end at the same heliocentric distance. The dots mark the same simulated time, i.e. the final time for the high-U_0 simulations and half the final time for the low-U_0 simulations. The dotted, dashed, solid black curves are the isocontours of growth rates $\gamma/\Omega_{ce} = 0.001, 0.1, 0.2$ for the resonant (i.e. oblique) EFI, from Gary & Nishimura (2003).

In Figure 4 we show the evolution of the radial (solid lines) vs transverse (dash-dotted lines) thermal velocities as a function of radial distance (bottom axis) and time (top axis), again for the four simulations mentioned before. The color code is the same as in Figure 3 and Table 1. Panel a and b refer to the high- and low-U_0 simulations respectively. The thermal velocity components are obtained by fitting with a bi-Maxwellian distribution the eVDF obtained from the simulation for the entire domain at selected, equally spaced times. A bi-Maxwellian fit is appropriate in the early stages of the simulations, before the onset of the instability. We will see later, in Figure 7 and Figure 8, how the eVDFs are modified, with respect to the bi-Maxwellian assumption, by the EFI onset. In future work, we will explore the suitability of fitting the simulation eVDF with other functions, such as kappa or flat-top distributions (Maksimovic et al. 2005; Wilson III et al. 2019).

The green lines in Figure 4 mark the double-adiabatic evolution for the transverse velocity component. The radial thermal velocity component is unaffected by double-adiabatic expansion. In this Figure, the instability onset is marked by a vertical line drawn at the last saved data point when the transverse thermal velocity component matches double-adiabatic prescription (notice that particle data, used to build the VDFs and hence to calculate the thermal velocities here, are saved at lower frequency with respect to field data). After that, the transverse velocity components start increasing: perpendicular heating due to firehose instability has started. Correspondingly, the radial velocity component starts decreasing significantly, due to firehose parallel cooling (Messmer 2002).

If we compare instability onset (i.e., departure from the green lines) in Figure 4 and 3, we see that the onset and nonlinear evolution of the EFI are efficient in bounding both the temperature anisotropy and the parallel plasma beta. The observed, reduced increase of $\beta_{\|,e}$ after the instability has started is due to parallel cooling. In fact, the mean value of the radial magnetic field component and of the plasma density are not affected by the emergence of EFI-related magnetic field fluctuations: they both keep decreasing as R^{-2}. Hence, the key component in the trend variation of the parallel beta is the parallel electron thermal velocity: it was constant before instability onset, it decreases after. Hence, the electron parallel beta after instability onset increases at a slower rate than before.

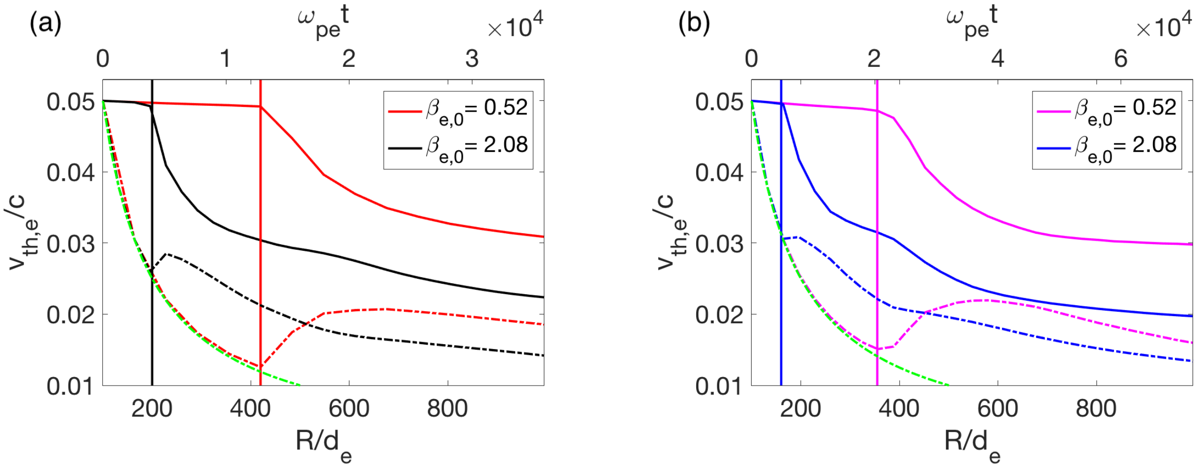

Figure 4. Evolution of the radial (solid lines) and transverse (dashed-dotted lines) electron thermal velocity components in the high-U_0 (panel a) and low-U_0 (panel b) simulations as a function of heliocentric distance (bottom axis) and time (top axis). The color code is the same as in previous Figures. The green lines mark double adiabatic expansion. After the vertical lines ($R/d_e \sim 420, 196, 356, 164$ for the red, black, magenta and blue simulations respectively), oblique firehose instability develops.

Let us now focus again on the high-beta simulations. At the final value of heliocentric distance, $R_f/d_e \sim 1000$, the particles in these simulations have spent more time in the firehose-unstable region than their lower beta counterparts, because the instability threshold was crossed at lower Rs. In both Figure 3 and Figure 4 we observe a similar behavior for the high-beta simulations: the temperature anisotropy is first reduced by the instability onset, and a first maximum after instability onset in Figure 3 is observed. Then, the transverse velocity starts decreasing again more rapidly than the radial one: the thermal anisotropy increases again, with a slope in Figure 3 quite close to that observed during adiabatic expansion. Then the trend reverses, and anisotropy again decreases: a second maximum in Figure 3 is reached by the blue simulation, and we can see a comparable trend in the black one. This behavior is quite similar to that observed in Figure 5 in Camporeale & Burgess (2008). There, it was explained as firehose instability bringing the simulation from the unstable area to marginal stability. After reaching stability, the development of a damping mode was observed, which brought the bulk parameters of the plasma back into unstable region, with the development of another, lower wavenumber and lower propagation angle firehose mode. The behavior we observe in our simulations is comparable, but the competition is not between firehose instability (pushing towards marginal stability) and damping modes (making the simulation unstable again), but rather between EFI and plasma expansion. Expansion, in fact, pushes the simulation towards larger temperature anisotropies and larger betas after a firehose mode has stabilized.

As a result, a new, lower angle, lower wavenumber EFI mode is destabilized. Competition between expansion and ion firehose instability has been shown by Hellinger & Trávníček (2008) in hybrid EBM simulations.

This competition is visible also in Figure 5, where we plot the evolution with heliocentric distance of the energy of the magnetic field oscillations for the four simulations. The values are normalized to the energy of their respective mean radial magnetic field components, which evolves as R^{-4}. From the Figure, we see an increase in magnetic field oscillation energy due to the development of the firehose instabilities after instability onset in all four cases. A peak is then reached, followed by a slight decrease in the energy ratio and then by a secular increase in the low beta simulations. In the blue case (high beta, low speed case), the saturation of the first unstable mode is followed by a new increase of the oscillation energy, a consequence of the destabilization of a second unstable mode. Secular growth follows the saturation of the second mode. In the black case (high beta, high speed), the destabilization of the second unstable mode transitions seamlessly into secular growth. The absence of a dip after the growth of the second unstable mode and a quite robust secular growth rate bring the energy ratio to the remarkable value of 0.4 (and growing) at the end of the simulation. Secular growth of magnetic field oscillation energy after the saturation of an unstable ion firehose instability mode has been reported in hybrid EBM simulations (Matteini et al. 2006; Hellinger & Trávníček 2013) and in hybrid simulations where pressure anisotropy is driven by a persistent linear shear in the magnetic field (Kunz et al. 2014).

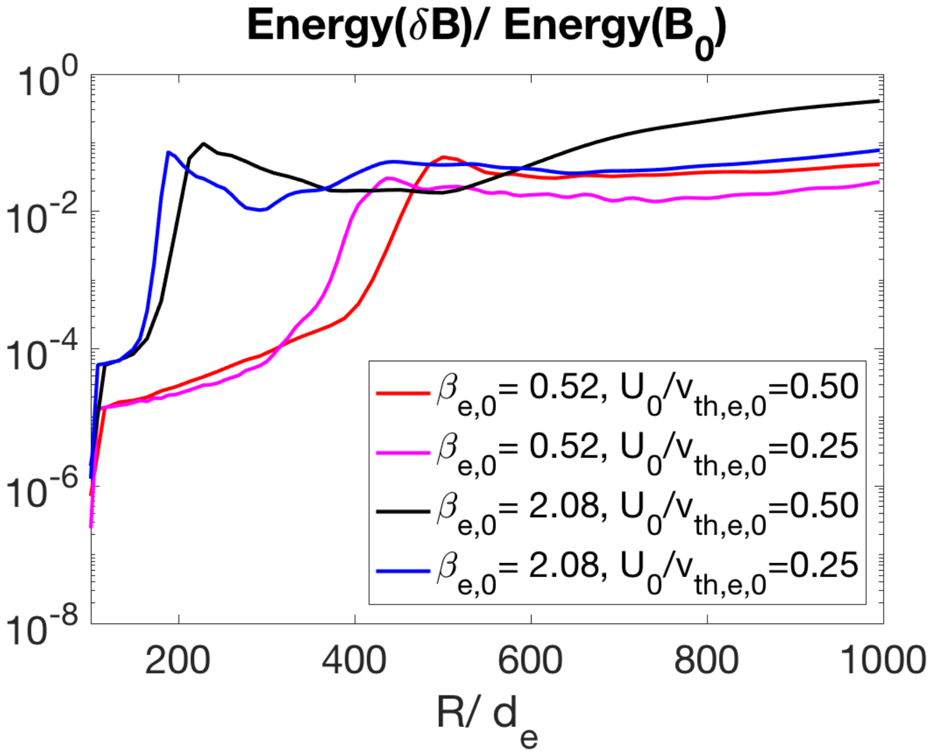

Figure 5. Evolution with heliocentric distance of the magnetic field oscillations. The value is normalized to the mean energy of the radial magnetic field component.

Going back to Figure 1, we observe that, starting from $R/d_e \sim 300$, the δB_x oscillations in panel d, appear to migrate to longer wavelengths, in a process culminating in the second maximum in $T_{\perp,e}/T_{\parallel,e}$ at about half the simulated time (dot in Figure 3). Figure 6 adds new details to the picture.

In Figure 6 we plot in panel a and b the FFT of the oscillations of the radial magnetic field component (the mean value, evolving as R^{-2}, has been removed) as a function of the radial, $k_x d_e$, and transverse, $k_y(R)d_e$, wavenumbers at different heliocentric distances, $R/d_e = 316$ and $R/d_e = 500$, for the simulation with $\beta_{e,0} = 2.08$, $U_0/v_{th,e,0} = 0.25$ (panel d in Figure 1). We have zoomed on the lower wavenumber areas and kept into account that the box expands in the transverse directions only: to calculate the angle of propagation of one mode, we have to consider that transverse wavenumbers translate to lower value because of the expansion.

At $R/d_e = 316$, we see that two modes are present, with propagation angles with respect to the background magnetic field direction of $\theta \sim 51°$ and $\theta \sim 68°$ respectively. At $R/d_e = 500$, the mode with larger propagation angle has been stabilized, as expected from the non expanding case (Camporeale & Burgess 2008). The mode energy has been dissipated into electron heating. The lower-angle, "surviving", mode has been shifted to lower propagation angles with respect to $R/d_e = 316$, as a consequence of the shifting of transverse wavenumbers to lower values due to the expansion. In Figure 6, panel c and d, we show the B_x magnetic field component at the same heliocentric distances as in panel a and b. Comparing panel c and d, we can notice at a glance in panel d the pattern simplification than comes from stabilizing the higher wavenumber modes, and that the oscillation wavelength in the trasverse direction is now larger then before. Figure 2 panel d adds a third, earlier, data point to the series, that allows to better visualize the migration of the unstable wavenumber to lower propagation angles and values, both in the transverse and radial direction.

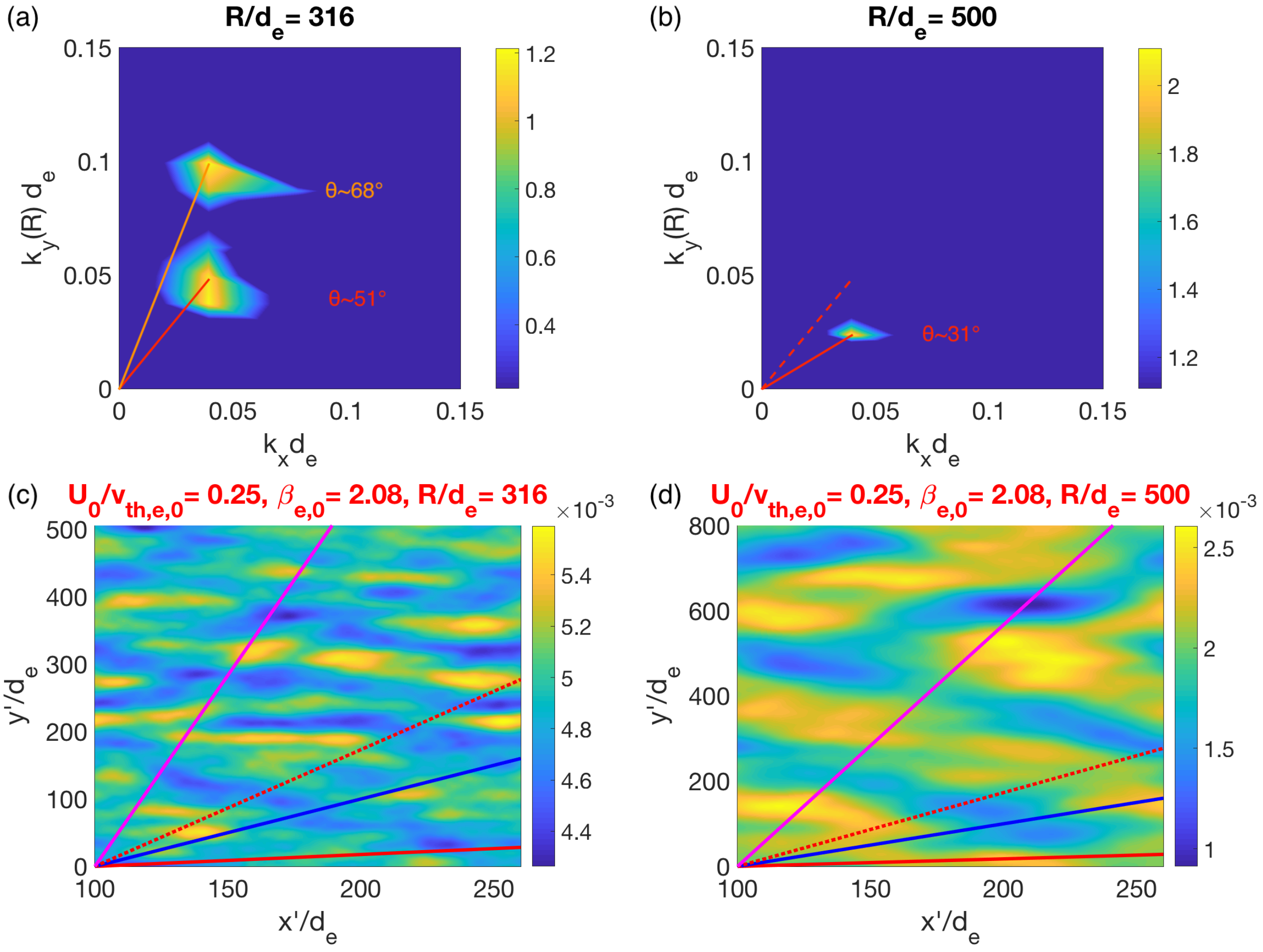

Figure 6. panel a and b: FFT of the oscillations of the radial magnetic field, δB_x (the mean value has been removed), at $R/d_e = 316$ (panel a) and $R/d_e = 500$ (panel b) for the simulation with $\beta_{e,0} = 2.08$, $U_0/v_{th,e,0} = 0.25$ (blue lines in Figure 3 and Figure 4). The stabilization of the mode with larger propagation angle and the shift of the surviving mode to lower propagation angles due to the expansion are both evident comparing the two panels. In panel c and d, B_x magnetic field component at the same heliocentric distances, as a function of the *Sun-centered* coordinates.

3. ELECTRON VELOCITY DISTRIBUTION FUNCTION EVOLUTION

Matteini et al. (2006) and Hellinger & Trávníček (2008) have shown the characteristic shape that ion VDFs assume when the ion firehose instability (parallel and oblique) is triggered in an expanding plasma. Similar dynamics are at work here. We focus now on some relevant stages of the evolution of the eVDF in the high speed, low and high-beta, simulations, paying attention to the competition between EFI perpendicular heating and expansion perpendicular cooling.

Let us focus on the high-speed simulations. In Figure 1 and Figure 4, panel a, we had marked at $R/d_e \sim 420, 196$ the last "CGL-compatible" point for the simulation with low (red) and high (black) beta respectively. We show now the v_x/c vs v_y/c eVDF at those (panel a) and at subsequent heliocentric distances for the low-beta (Figure 7) and for the high-beta (Figure 8) case. In both cases, panels b and c are the first EFI-unstable eVDF and the one recorded just after. Panels d is the last eVDF available for each simulations.

Moving from panel a to b in Figure 7 and Figure 8, and hence from the "last stable" to the first "firehose unstable" eVDFs, we notice the expected perpendicular heating we already remarked upon in Figure 4, panel a. The green lines in panel b to d are drawn at the $v_\parallel(R) \sim \pm\Omega_{ce}(R)/\sqrt{2}k_x d_e(R)$ values at which resonant interaction is expected. We notice that, in calculating the value of expected interaction, we have kept into account the variation of both the electron cyclotron frequency and of the electron skin depth with heliocentric distance. The specific k_x value used in this calculation is obtained from the FFT of δB_x, and is different for the two cases: $k_x d_e \sim 0.04, 0.11$ for the low-beta and high-beta simulations respectively. As we have already noticed, the wavenumber at instability onset for the high-beta simulations is higher than for the low-beta simulations.

In both panels b, the green line well identifies the high $|v_x|/c$ population perpendicularly heated by the firehose instability. In Figure 7, it clearly separates the perpendicularly heated population from another, low $|v_x|/c$ population where expansion cooling is still quite visible. In Figure 8, we see that the green lines map well to the non Maxwellian shape of some of the eVDF contours, see the red arrow. However, the clear separation between heated and cooled populations of Figure 7 is not seen here. This is due to two factors: first, instability onset in the high-beta simulation occurred at lower R than in the low-beta case, hence perpendicular cooling was less evident in the eVDF pre-instability (compare panel a and b in the two Figures). Second, in the high-beta simulation the time scale of the instability is faster, the growth rate is higher. Hence, the process that brings the resonant eVDFs back to a bi-Maxwellian-like shape is faster in the high-beta simulations, and blurs the separation between the cold and hot electrons. This process can be fully appreciated in the video depicting the eVDF evolution with heliocentric distance in the low-beta, high-speed simulation, "HighU0LowBeta.avi" and in Figure 7, panel c to d. There we see that, after instability onset, the heated particles are deflected over resonant surfaces towards lower $|v_x|/c$ values and "close the gap" at low $|v_x|/c$ separating perpendicularly heated and cooled particles.

This same process must happen in the high-beta case on a time scale shorter than the temporal difference between Figure 8, panel a and b, and covers the formation of a clearly defined butterfly shape.

It is important to remark that in all cases examined here, at the end of the simulation (panel d in Figure 7 and Figure 8), the more specifically resonant features of the eVDF (e.g., the butterfly shape in Figure 7) have been replaced by more "bi-Maxellian like" eVDFs. The peculiar resonant appearance of the eVDF is then a transient feature, but there is little doubt that, as expected from literature, resonant wave particle interaction is responsible for perpendicular heating in these oblique simulations.

4. DISCUSSION AND CONCLUSIONS

In this paper, we have presented fully kinetic simulations of the oblique electron firehose instability in expanding plasmas. This work contributes to the understanding of the evolution of the electron energy balance with heliocentric distance. Štverák et al. (2015) has demonstrated, through the analysis of electron properties in the fast and slow solar wind between 0.3 and 1 AU, that external heating terms are not required for electrons which, on the contrary, exhibit negative cooling rates. Mechanisms to transport energy from the parallel to the perpendicular direction are however required to match the observed temperature radial trends. The resonant electron firehose instability may be one of these mechanisms.

The simulations are performed with the newly developed, fully kinetic, semi-implicit, Particle In Cell, Expanding Box Model code EB-iPic3D (Innocenti et al. 2019).

The four simulations are characterized by different electron parallel beta and different background solar wind speed at initialization. The two background solar wind speeds roughly map to slow ($\sim$ 400 km/s) and very fast ($\sim$ 800 km/s) solar wind. Štverák et al. (2008) confirms that both beta/ temperature ratio couples are compatible with actual observed values.

The main novelties of this paper with respect to previous literature on the electron firehose instability (EFI) in the solar wind are: first, the instability arises self-consistently after a phase of double-adiabatic, CGL-like expansion. This

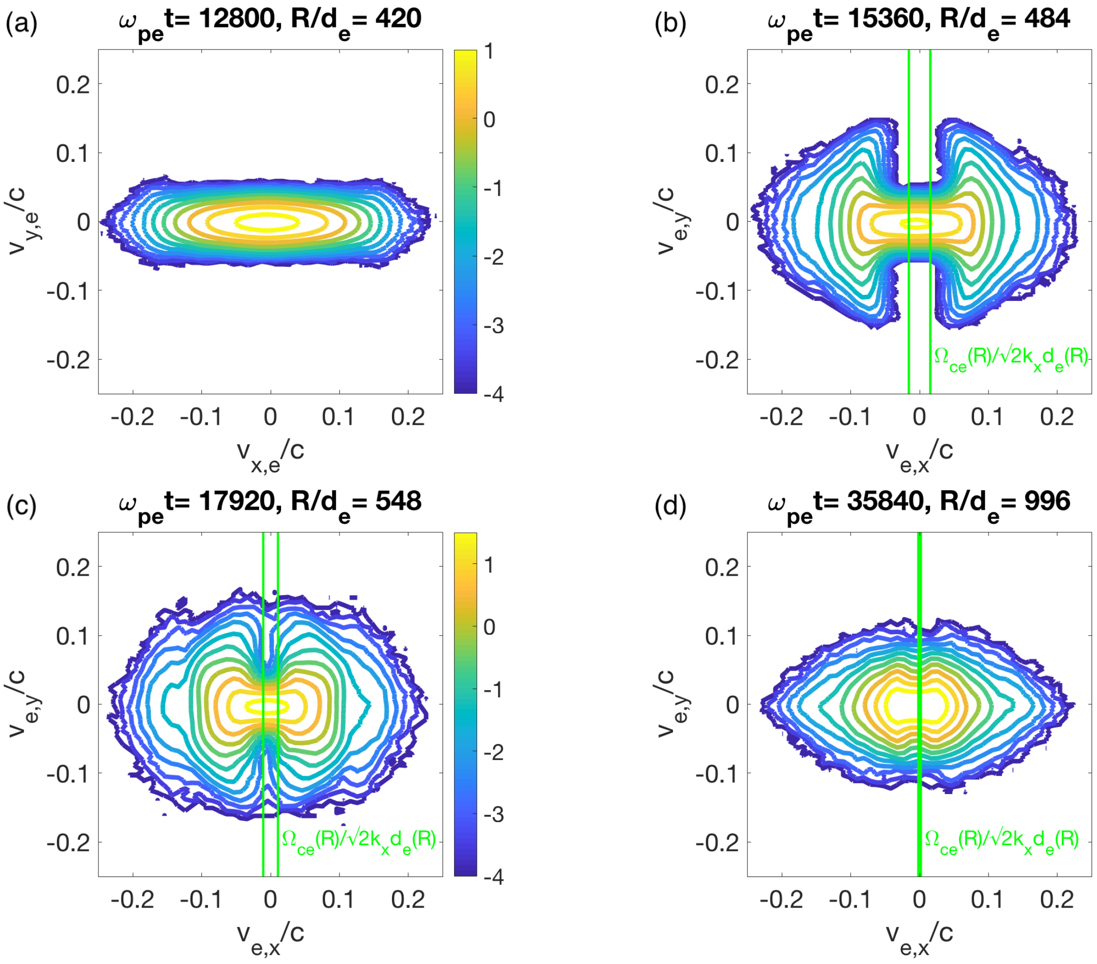

Figure 7. Electron eVDF (v_x/c vs v_y/c plane, with x the radial direction) for the high-speed, low-beta simulations, just before (panel a) and after (panel b, c, and d) the onset of the firehose instability. The vertical lines are drawn, after instability onset, at the parallel velocity values at which anomalous Doppler resonance is expected, $v_\parallel \sim \pm\Omega_{ce}(R)/\sqrt{2}k_x d_e(R)$.

confirms that EFI can arise in solar wind plasmas due to the modification of the bulk parameters (perpendicular to parallel temperature ratio and electron parallel beta) due to plasma parcel expansion; second, and most important, since the plasma expansion continues after the onset of the EFI, our simulations allow to observe how expansion and instability compete in shaping solar wind parameters.

All simulations are initialized with isotropic electron and ion velocity distribution functions. This choice does not reflect real solar wind conditions, where kinetic features in the electron velocity distribution function are present possibly already in the corona (Pinfield et al. 1999; Esser & Edgar 2000; Chiuderi & Drago 2004) and surely at larger heliocentric distances. It is however a good starting point at this stage of our investigation, since it allows to distinguish the effects of the electron firehose instability from those of other, concurrent processes at work in the real solar wind.

In the double-adiabatic, CGL-like, phase, the electron temperature ratio and the electron parallel beta increase with the heliocentric distance R as $T_{\parallel,e}/T_{\perp,e}, \beta_{\parallel,e} \propto R^2$, until the threshold for the onset of the oblique firehose instability is crossed, see Figure 3.

We remark at this point that EBM simulations are useful also in terms of understanding which, of competing instabilities, is the preferred channel for perpendicular electron heating in the solar wind. In particular, we address here the issue of the competition between firehose and magnetized Weibel instability (WI) in theory and in our simulations. Lazar et al. (2010) compares the marginal stability threshold of the parallel firehose instability (whose threshold is higher than for the oblique) with that of the magnetized WI. Notice that, in Lazar et al. (2010), firehose instability really means *parallel* firehose instability, hence the "non resonant" in the title (quite high temperature

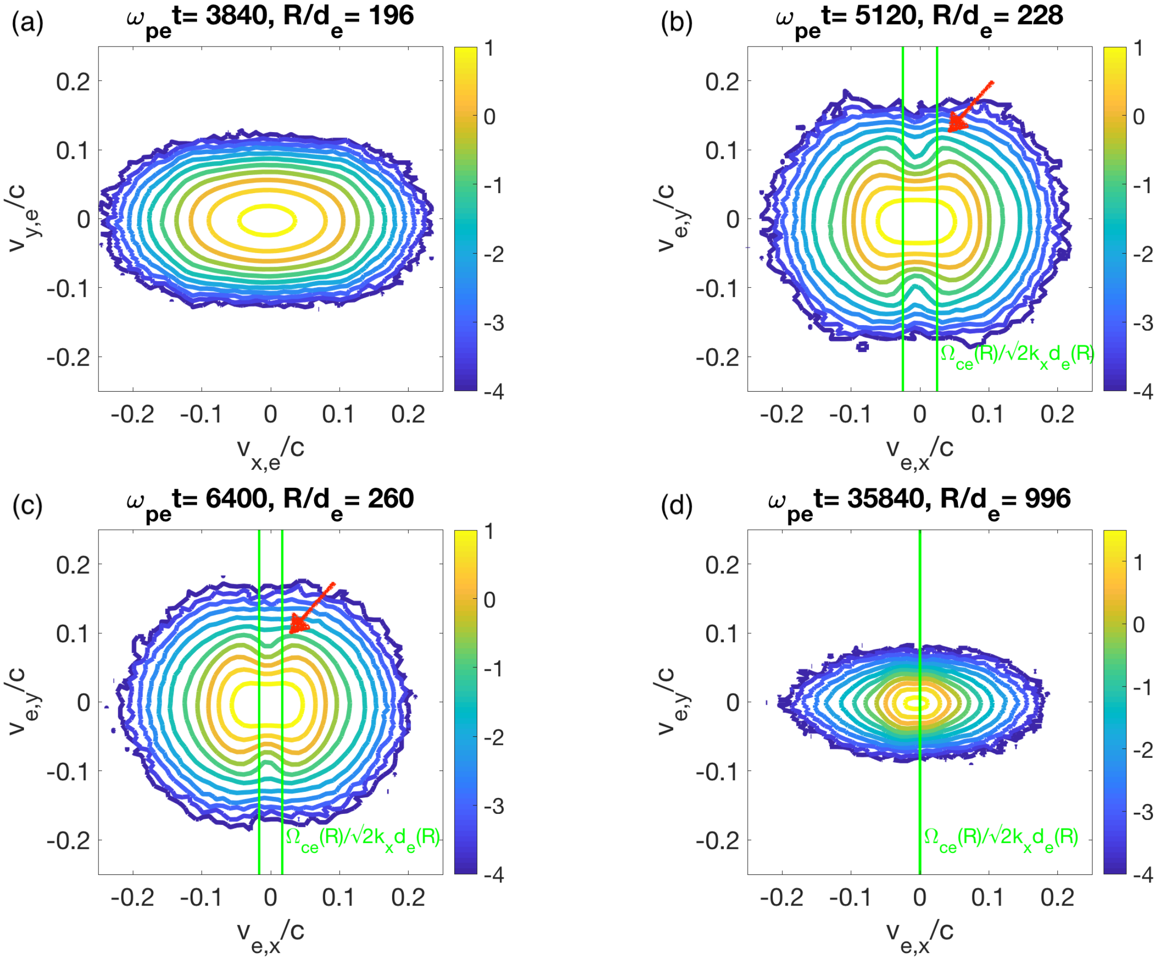

Figure 8. Electron eVDF (v_x/c vs v_y/c plane, with x the radial direction) for the high-speed, high-beta simulation, just before (panel a) and after (panel b, c, and d) the onset of the firehose instability. The vertical lines are drawn, after instability onset, at the parallel velocity values at which anomalous Doppler resonance is expected, $v_\parallel(R) \sim \pm\Omega_{ce}(R)/\sqrt{2}k_x d_e(R)$.

anisotropies are needed for the parallel EFI to become resonant). The WI marginal stability curve falls below the EFI curve, meaning a plasma expanding double adiabatically should reach the EFI unstable zone before the WI unstable zone. To check this assumption, we have run convergence tests with box sizes $L_x/d_e = L_y/d_e = 10, 20, 40, 80$. Under such conditions, a magnetized Weibel instability, rather than an oblique firehose instability, develops, since the rather low wavenumber characterizing the EFI are not accessible with these smaller box sizes. Compatibly with the conclusions of Lazar et al. (2010), we observe that, with the same plasma parameters as in our high-speed, low-beta case, $U_0/v_{th,e,0} = 0.5$ and $\beta_{e,0} = 0.52$, the magnetized Weibel instability arises after a longer phase of adiabatic expansion (the instability threshold is higher), at $\beta_{\parallel,e} > 18$, where $T_{\perp,e}/T_{\parallel,e} \sim 0.044$. Perhaps as a consequence of the later onset, this instability is less efficient than the EFI in limiting the temperature anisotropy ratio, which is, at its lowest value after the onset of the instability, $T_{\perp,e}/T_{\parallel,e} \sim 0.18$ and at $R/d_e \sim 1000$ (the same final heliocentric distance as the firehose simulations), $T_{\perp,e}/T_{\parallel,e} \sim 0.15$. Apart from the larger threshold, we observe other differences between EFI and WI: a difference of scale (WI wavenumbers are higher), of propagation angle (the WI is purely perpendicular) and of eVDF shape after instability onset. The very characteristic deformation due to wave-particle resonance is lost, since WI heats electrons in a non-resonant, non $v_\parallel$-specific fashion.

As we noticed already, the main point of interest of expanding box EFI simulations is the possibility of simulating from first principles the competition of electron firehose and adiabatic expansion in shaping solar wind parameters.

In non expanding plasmas, the electron firehose instability acts in the direction of reducing electron thermal anisotropy, reducing the electron parallel beta, shifting the unstable modes from higher to lower wavenumbers and reducing the angle of propagation with respect to the background magnetic field (Camporeale & Burgess 2008). On the contrary, double adiabatic expansion tends to increase both the temperature anisotropy and the electron parallel beta. The angle of propagation with respect to the radial direction of an unstable mode in an expanding box is progressively reduced by the shift of the transverse wavenumbers to lower values, as a consequence of larger transverse box sizes.

When the firehose and the expansion shape the bulk plasma properties together, a compromise is reached in terms of anisotropy and electron parallel beta evolution. With EFI, the thermal anisotropy is lower than it would be in pure CGL, thanks to the firehose perpendicular heating and parallel cooling (perpendicular heating and parallel cooling processes from kinetic instabilities in the solar wind are actually some of the reasons why the CGL approximation does not hold there). We also observe that the EFI is particularly efficient in locking the parallel beta, which continues to increase, but at a much lower rate than it would in purely adiabatically expanding plasmas. While the decrease in parallel plasma pressure is not sufficient to contrast the faster decrease with R of the magnetic field pressure, it is quite efficient in limiting an otherwise faster increase in $\beta_{\parallel,e}$.

We observe the competition between EFI and adiabatic expansion also in the shape of the eVDFs after the onset of the instability. In the low-beta case in particular, where the instability onset occurs at larger heliocentric distances, we can observe a clear separation between the high $|v_x|/c$ population perpendicularly heated by the instability through resonant processes and a lower-$|v_x|/c$ population where adiabatic cooling is still visible. The characteristic gap in the butterfly EFI eVDF shape is then closed at larger heliocentric distances by deflection of the heated electrons over resonant surfaces and, at large distances from instability onset, the character of the eVDF is closer to bi-Maxwellian.

Looking at the trajectories of the simulation in the $T_\perp/T_\parallel$ vs $\beta_\parallel$ plane of Figure 3, we see another aspect of the competition between EFI and expansion: when a firehose mode stabilizes, the expansion pushes the plasma again in a firehose unstable area. The new mode has larger wavenumber, lower propagation angle with respect to the one that saturated. This process mimics the competition between firehose and damping modes in non expanding plasmas, and points to a rather efficient, self-perpetuating perpendicular heating mechanism in the solar wind.

We have already noticed that, in Figure 3, the slower-wind simulations are closer to the marginal stability limits than the faster-wind simulations. This is consistent with Štverák et al. (2008), which observes that the firehose instability marginal instability contours bound the slow wind better than the fast wind.

We observe two major differences between our trajectories in the $T_\perp/T_\parallel$ vs $\beta_\parallel$ plane and those observed in Štverák et al. (2008).

First, solar wind observations are all in the firehose-stable area of the plane. Our simulations start in the stable area and, as expected, are brought by expansion into the EFI-unstable area. Once there, onset and non linear evolution of the EFI bring them closer to the marginal stability contour than at instability onset. However, they never cross into the stable region.

Second, in Štverák et al. (2008), no migration in the $T_\perp/T_\parallel$ vs $\beta_\parallel$ plane is observed as a function of heliocentric distance. When comparing slow wind, core electrons (incidentally, the population better bound by the EFI marginal stability contour) at 0.35, 0.5, 1 and 2 AU, no substantial difference in parallel electron beta is observed (but in Berčič et al. (2019), an increase in parallel electron beta with heliocentric distance is registered for halo electrons). This is in contrast with what we observe in our simulations, where parallel beta keeps increasing also after instability onset, and with observations of the ion population at different heliocentric distances: in Matteini et al. (2013), Helios (0.3 AU) and Ulysses (>1 AU) proton measures occupy quite distinct regions in the ion $T_\perp/T_\parallel$ vs $\beta_\parallel$ plane, with Ulysses observations having larger parallel betas. The electron observations in Štverák et al. (2008) point to either parallel cooling able to stave off parallel beta increase (hence, $v_{th,x} \propto R^{-1}$, assuming that density and magnetic background magnetic field keep evolving, CGL-like, as R^{-2}), or to a departure of the evolution of the background density and radial magnetic field from R^{-2} (notice that the background magnetic field is expected to move to an R^{-1} dependance when the transverse component becomes dominant). In our simulations, where the magnetic field is purely radial,, we see a slower decrease of $v_{th,x}$ with heliocentric distance and both density and radial magnetic field decrease with R as R^{-2}.

Ongoing investigations suggest that the reason for both these differences lie in our choice of initial conditions, which can definitively be made more realistic. At the moment, our electrons are composed of a single, isotropic population; the simulations box, while large enough to accommodate EFI dynamics, could be made larger to accommodate lower-wavenumber modes possibly capable of further extracting energy from the eVDF; the introduction of a transverse initial magnetic field component may give rise to more realistic electron dynamics. Ongoing work shows that a more realistic description of the initial magnetic field gives simulation results more in line with observations, i.e. able to reach the EFI marginal stability limit and to lock the increase of the parallel electron beta.

At this stage, however, we should remark that reaching EFI marginal stability is only a first step. As remarked in Yoon & Sarfraz (2017), one of the outstanding issues in solar wind physics is why, in the above mentioned $\beta_\parallel$ vs $T_\perp/T_\parallel$ plots of both ion and electron observations, the majority of the data points lies far away from the marginal stability boundaries of the limiting instabilities. In Yoon & Sarfraz (2017) the evolution of solar wind plasma parcels in term of the ion and electron $\beta_\parallel$ vs $T_\perp/T_\parallel$ plots is shown, for different electron and ion initial parameters. The trajectories are calculated by solving in a quasi-linear framework and as a function of the heliocentric distance a system of equations that factors in plasma expansion and the effects on the magnetic field and temperature anisotropies of parallel, left-hand circularly polarized modes, namely the parallel EFI and the electromagnetic ion cyclotron instability (EMIC). It is shown that, while electron-ion interaction mediated by EFI and EMIC is successful in bringing the ion population far away from the upper and lower marginal stability boundaries and well into the stable area, the electron population seems to be more closely bounded to the EFI boundary (incidentally, cycles of EFI stabilization and de-stabilization due to the interplay between instability and expansion are observed there).

As advocated in the conclusions of Yoon & Sarfraz (2017), we plan on using our fully kinetic expanding box code to explore further mechanisms for electron perpendicular heating, possibly capable of better reproducing observations in the stable region.

As observed in Table 1, the solar wind is a subsonic flow for electrons. Concerns may arise from the fact that, at this stage, our model does not address the specific challenges that the evolution of a subsonic species entails, with respect to a supersonic one. The reason is that, if the wind speed is subsonic, a large number of particles exist that are moving at substantially different speeds with respect to the box, including a large fraction of particles moving backwards towards the Sun. Therefore, the VDF of a subsonic species in the expanding solar wind is modified, with respect to CGL expectations, by its subsonic nature and by wave/particle interaction. If no wave-particle interactions are aroud, the solution to the evolving VDF follows Jeans' theorem: Landi et al. (2012) shows, in their Figure 2, that when a subsonic population is left to expand *in absence of any interaction*, significant VDF deformation may ensue. However, such VDFs are dramatically unstable, a feature that is the focus of our simulations.

A simple experiment can illustrate these effects. We run a non expanding box simulation initialized with the same parameters as the high-speed, high-beta simulation discussed previously. Instead of using isotropic electrons (thin black lines in Figure 9) and ions as initial conditions, we initialize particles using the prescription from the above-mentioned Figure 2 of Landi et al. (2012), depicted in Fig. 9, panel a, thick color lines, assuming $R/R_0 = 2$. We remark that this is not a realistic solar wind VDF, but the VDF that would develop letting a sub-sonic population expand in absence of particle/ particle, wave / particle interaction. The VDF shown in thin, color lines modifies only the perpendicular velocity values, as $1/R$, and is drawn for comparison. Our code produces something very similar to that (minor modifications come from wave/particle interaction) at $R/d_e = 200$.

The simulation so initialized is left to evolve, and, as expected, the VDF is self-consistently modified towards a more stable configuration. In panel b, color thick lines, we show the VDF at $\omega_{pe}t = 300$, which corresponds to $R/d_e = 208$, $\Delta R/R_f = 0.008$, where R_f is the final heliocentric distance reached in the previously shown EB simulations. After that time, no macroscopic modifications of the VDF are observed up to the end of the run, $\omega_{pe}t = 800$. The EFI does not develop yet, consistently with the fact that the EB simulation, at $R/d_e = 200$, was not EFI-unstable.

We notice that after quite a short time, the most striking, non Maxwellian features of the "sub-sonic VDF" are eliminated by wave/particle interaction, and the resulting VDF is relatively similar to the anisotropic Maxwellian that would develop in our EB simulation. We conclude that wave/ particle interaction (in our code, but even more so in the real solar wind) acts in the direction of mitigating the more extreme VDF features in sub-sonic species, and therefore our misrepresentation of electron motion can be considered limited. We leave further, more quantitative studies to future work.

In the meanwhile, our confidence in the validity, at least in the statistical sense, of the results we present in this paper is boosted by comparison with observations. As evident from Štverák et al. (2008), in fact, solar wind electron observations are compatible with the evolution of the electron firehose instability. Furthermore, also analytical investigation, e.g. Yoon & Sarfraz (2017) supports the main evolution picture we are drawing.

Up to now the main obstacle to the use of more realistic initial conditions (especially in terms of electron and ion VDFs) was the lack of relevant observations at low heliocentric distances: before 2018, the points of closest approach to the Sun were the Helios spacecrafts, which reached ~ 0.3 AU. As we already observed, isotropic, single population

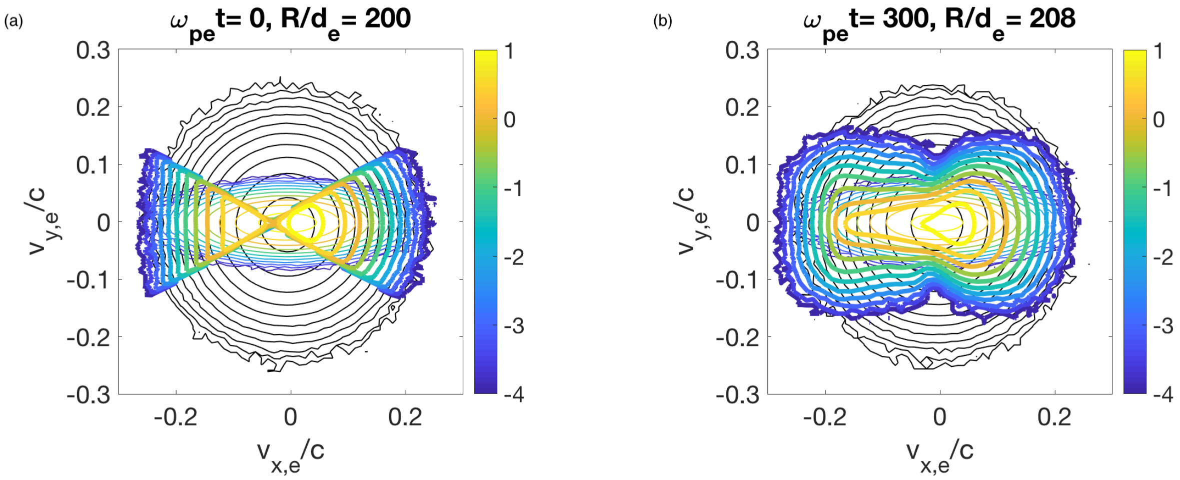

Figure 9. Panel a and b: Isotropic electron VDF (thin black line) and VDF at $R/R_0 = 2$, assuming $v_\perp = v_{perp,0}R_0/R$ (color thin line). The latter is the expected electron VDF after an EB-iPic3D run up to $R = 2R_0$. Panel a, color thick lines: “sub-sonic VDF” evolved with Jeans’ theorem in absence of any interaction up to $R = 2R_0$, used as initial condition for the run. Panel b: the simulated VDF, after the initial ”sub-sonic VDF” is left to evolve in a non expanding box PIC simulation for $\omega_{pe}t = 300$. The most striking non Maxwellian features have been normalized away.

electron and ion VDFs are a good starting point, but such a choice risks suppressing instabilities that may arise in the solar wind due to the interaction of different, non isotropic, particle populations. Luckily, 0.3 AU is not anymore the distance of closest approach to the Sun.

Parker Solar Probe, PSP (Fox et al. 2016), has been launched in August 2018, and is currently orbiting the Sun. Encounters with Venus will provide gravity assists that will send it on an orbit with perihelia closer and closer to the solar surface, down to ∼ 9 solar radii. PSP is equipped with two electrostatic analyzers and a Faraday cup (SWEAP, Solar Wind Electrons Alphas Protons, instruments) which will provide high-resolution velocity distribution functions for electrons, protons and helium ions. Future work will use such observed electron and ion VDFs as initial conditions for more realistic simulations.

The authors would like to thank Petr Hellinger, Shaaban Mohammed Shaaban and Alfredo Micera for useful discussions. M.E.I.’s research is supported by an appointment to the NASA Postdoctoral Program at the Jet Propulsion Laboratory, administered by Universities Space Research Association under contract with NASA. M.V. and A.T. acknowledge support from the NASA LWS grant NNX15AF34G. M.E.I. is an FWO postdoctoral fellow currently on leave.

REFERENCES

Ahmadi, N., Germaschewski, K., & Raeder, J. 2017, Physics of Plasmas, 24, 122121

Behannon, K. W. 1978, Reviews of Geophysics, 16, 125

Berčič, L., Maksimović, M., Landi, S., & Matteini, L. 2019, Monthly Notices of the Royal Astronomical Society, 486, 3404

Brackbill, J., & Forslund, D. 1982, Journal of Computational Physics, 46, 271

Camporeale, E., & Burgess, D. 2008, Journal of Geophysical Research: Space Physics, 113

Chew, G., Goldberger, M., & Low, F. 1956, Proceedings of the Royal Society of London. Series A. Mathematical and Physical Sciences, 236, 112

Chiuderi, C., & Drago, F. C. 2004, Astronomy & Astrophysics, 422, 331

Daughton, W., Roytershteyn, V., Albright, B. J., et al. 2009, Phys. Rev. Lett., 103, 065004. https://link.aps.org/doi/10.1103/PhysRevLett.103.065004

Dong, Y., Verdini, A., & Grappin, R. 2014, The Astrophysical Journal, 793, 118

Esser, R., & Edgar, R. J. 2000, The Astrophysical Journal Letters, 532, L71

Feldman, W., Asbridge, J., Bame, S., Montgomery, M., & Gary, S. 1975, Journal of Geophysical Research, 80, 4181

Fitzenreiter, R., Ogilvie, K., Chornay, D., & Keller, J. 1998, Geophysical research letters, 25, 249

Fox, N., Velli, M., Bale, S., et al. 2016, Space Science Reviews, 204, 7

Gary, S. P. 2005, Theory of space plasma microinstabilities (Cambridge university press)

Gary, S. P., & Nishimura, K. 2003, Physics of Plasmas, 10, 3571

Grappin, R., & Velli, M. 1996, Journal of Geophysical Research: Space Physics, 101, 425

Hammond, C., Feldman, W., McComas, D., Phillips, J., & Forsyth, R. 1996, Astronomy and Astrophysics, 316, 350

Hellinger, P., Matteini, L., Landi, S., et al. 2015, The Astrophysical Journal Letters, 811, L32

Hellinger, P., Matteini, L., Štverák, Š., Trávníček, P. M., & Marsch, E. 2011, Journal of Geophysical Research: Space Physics, 116

Hellinger, P., Trávníček, P., Kasper, J. C., & Lazarus, A. J. 2006, Geophysical research letters, 33

Hellinger, P., Trávníček, P., Mangeney, A., & Grappin, R. 2003, Geophysical research letters, 30

Hellinger, P., & Trávníček, P. M. 2008, Journal of Geophysical Research: Space Physics, 113

—. 2013, Journal of Geophysical Research: Space Physics, 118, 5421

Hellinger, P., Trávníček, P. M., Decyk, V. K., & Schriver, D. 2014, Journal of Geophysical Research: Space Physics, 119, 59

Innocenti, M., Lapenta, G., Markidis, S., Beck, A., & Vapirev, A. 2013, Journal of Computational Physics, 238, 115 . http://www.sciencedirect.com/science/article/pii/S0021999112007590

Innocenti, M., Norgren, C., Newman, D., et al. 2016, Physics of Plasmas, 23, 052902

Innocenti, M. E., Beck, A., Ponweiser, T., Markidis, S., & Lapenta, G. 2015, Computer Physics Communications, 189, 47

Innocenti, M. E., Lazar, M., Markidis, S., Lapenta, G., & Poedts, S. 2011, Physics of Plasmas, 18, 052104

Innocenti, M. E., Tenerani, A., & Velli, M. 2019, The Astrophysical Journal, 870, 66

Kunz, M. W., Schekochihin, A. A., & Stone, J. M. 2014, Physical Review Letters, 112, 205003

Landi, S., Matteini, L., & Pantellini, F. 2012, The Astrophysical Journal, 760, 143

Lapenta, G., Brackbill, J., & Ricci, P. 2006, Physics of plasmas, 13, 055904

Lazar, M., Poedts, S., & Schlickeiser, R. 2010in , AIP, 280–283

Li, X., & Habbal, S. R. 2000, Journal of Geophysical Research: Space Physics, 105, 27377

Liewer, P. C., Velli, M., & Goldstein, B. E. 2001, Journal of Geophysical Research: Space Physics, 106, 29261

Maksimovic, M., Pierrard, V., & Riley, P. 1997, Geophysical research letters, 24, 1151

Maksimovic, M., Zouganelis, I., Chaufray, J.-Y., et al. 2005, Journal of Geophysical Research: Space Physics, 110

Markidis, S., Lapenta, G., et al. 2010, Mathematics and Computers in Simulation, 80, 1509

Marsch, E. 2012, Space science reviews, 172, 23

Matteini, L., Hellinger, P., Goldstein, B. E., et al. 2013, Journal of Geophysical Research: Space Physics, 118, 2771

Matteini, L., Landi, S., Hellinger, P., & Velli, M. 2006, Journal of Geophysical Research: Space Physics, 111

Messmer, P. 2002, Astronomy & Astrophysics, 382, 301

Ofman, L. 2019, arXiv preprint arXiv:1903.11343

Ogilvie, K., & Scudder, J. 1978, Journal of Geophysical Research: Space Physics, 83, 3776

Paesold, G., & Benz, A. O. 1999, Astronomy and Astrophysics, 351, 741

Pilipp, W. G., Miggenrieder, H., Montgomery, M. D., et al. 1987, Journal of Geophysical Research: Space Physics, 92, 1075. https://agupubs.onlinelibrary.wiley.com/doi/abs/10.1029/JA092iA02p01075

Pinfield, D., Keenan, F., Mathioudakis, M., et al. 1999, The Astrophysical Journal, 527, 1000

Salem, C., Hubert, D., Lacombe, C., et al. 2003, The Astrophysical Journal, 585, 1147

Scime, E. E., Bame, S. J., Feldman, W. C., et al. 1994, Journal of Geophysical Research: Space Physics, 99, 23401

Sironi, L., & Narayan, R. 2015, The Astrophysical Journal, 800, 88

Štverák, Š., Trávníček, P., Maksimovic, M., et al. 2008, Journal of Geophysical Research: Space Physics, 113

Štverák, Š., Trávníček, P. M., & Hellinger, P. 2015, Journal of Geophysical Research: Space Physics, 120, 8177

Tenerani, A., & Velli, M. 2017, The Astrophysical Journal, 843, 26. http://stacks.iop.org/0004-637X/843/i=1/a=26

Velli, M., Grappin, R., & Mangeney, A. 1992in , AIP, 154–159

Verdini, A., & Grappin, R. 2015, The Astrophysical Journal Letters, 808, L34

—. 2016, The Astrophysical Journal, 831, 179

Weibel, E. S. 1959, Physical Review Letters, 2, 83

Wilson III, L. B., Stevens, M. L., Kasper, J. C., et al. 2018, The Astrophysical Journal Supplement Series, 236, 41

Wilson III, L. B., Chen, L.-J., Wang, S., et al. 2019, arXiv preprint arXiv:1902.01476

Yoon, P. H., & Sarfraz, M. 2017, The Astrophysical Journal, 835, 246